COMMUNICATION

Efficient and Color-Tunable Oxyfluoride Solid Solution Phosphors for Solid-State White Lighting

Won Bin Im, Nathan George, Joshua Kurzman, Stuart Brinkley, Alexander Mikhailovsky, Jerry Hu, Bradley F. Chmelka, Steven P. DenBaars,* and Ram Seshadri**

The past decade has seen rapid development in GaN-based light-emitting diode (LED) technology, especially focused on advanced solid-state white lighting sources.[1–4] To obtain white light from LEDs, strategies involve combining several LED chips of different colors, using quantum dots (QD) to down-convert higher energy light,[5–9] or using phosphors to down-convert near-UV and blue light. The phosphor approach has the advantages of high efficiency, long lifetimes, physical robustness, a mercury-free design, and color stability.[10] We recently reported a new green-emitting phosphor, $Sr_{2.975-x}Ce_{0.025}Ba_xAlO_4F$ ($SBAF:Ce^{3+}$). Although the quantum efficiency (QE) is nearly 100%, $SBAF:Ce^{3+}$ degrades upon contact with moisture, raising questions regarding stability in real-world applications.[11] Here, we prepare solid solutions between the nearly isostructural compounds Sr_3AlO_4F (SAF) and Sr_3SiO_5 (SSO), which yields the phosphor $Sr_{2.975}Ce_{0.025}Al_{1-x}Si_xO_{4+x}F_{1-x}$ ($SASF:Ce^{3+}$). The SSO end-member has been reported to have moisture stability and high QE.[12,13] Solid solutions between SAF and SSO give highly efficient (QE = 85% for $x = 0.5$), highly color-tunable (λ_{em} = 474 to 537 nm) phosphors with improved moisture stability that have great potential for use in solid-state white lighting. A new phosphor-capping method for white LEDs is also presented, which reduces light reflection to the LED chip and improves luminous efficacy by nearly a factor of two when compared to previous studies. Phosphor-converted solid-state lighting devices have been developed using the $x = 0.5$ $SASF:Ce^{3+}$ phosphor, which have an efficacy of 73 lm W^{-1} under a 20 mA forward bias with a color rendering index (R_a) of 69 and correlated color temperature (CCT) of 6937 K.

Along with possessing an appropriate excitation wavelength, solid-state phosphors must remain chemically and physically stable and resist thermal quenching at temperatures up to 200 °C.[10,15] Recent efforts to develop new LED phosphors include oxide,[16–21] oxyfluoride,[22,23] nitride,[24–27] oxynitride,[28–30] sulfide,[31,32] and halide[33,34] hosts. Despite many successes, continued efforts are required to address issues of higher efficiencies, better color rendition, and better thermal quenching characteristics. Currently, $Y_3Al_5O_{12}:Ce^{3+}$ is perhaps the most frequently used phosphor, but this material lacks thermal stability at elevated temperatures during white LED operation[35] and suffers a low R_a when pumped by a blue LED chip.[36]

We previously reported a solid solution between the phosphor host compound, $LaSr_2AlO_5$[37] and SSO,[38] as well as phosphor hosts from the solid solution of $GdSr_2AlO_5$ and SAF.[39] For $SASF:Ce^{3+}$, two substitutions occur across the solid solution series, both of anions (O^{2-} for F^-) and of cations (Si^{4+} for Al^{3+}), which impart superior phosphor properties. The Ce:Sr ratio in this family has been optimized at 0.025:2.975, from a knowledge of optimal concentrations for both end-members.[11,13] Note that the composition as reported here is not charge balanced, with an excess of 0.025 positive charges per unit cell. There are many ways that this excess positive charge can be compensated, for example, by a slight increase of the O/F ratio or cation vacancies. These compensating mechanisms would occur to extents not detectable by techniques used here.

The $SASF:Ce^{3+}$ phosphors have been characterized by using a combination of powder X-ray diffraction (XRD), solid-state ^{19}F NMR spectroscopy, synchrotron X-ray total scattering, and UV-vis spectroscopy. Optical property measurements show that $SASF:Ce^{3+}$ phosphors are bright and broad emitters under 430 nm excitation. $SASF:Ce^{3+}$ materials have been incorporated into phosphor-capped white LEDs using an InGaN LED chip (λ_{max} = 434 nm). This LED prototype has been optically characterized. Thermal quenching of the luminescence and analysis of the local structure of $SASF:Ce^{3+}$ with solid-state ^{19}F NMR and synchrotron X-ray total scattering suggest explanations for the unusual brightness of the new phosphor.

Dr. W. B. Im, Steven P. DenBaars, Prof. S. P. Seshadri
Solid State Lighting and Energy Center and Materials Department
University of California Santa Barbara
Santa Barbara, CA 93106 USA
E-mail: denbaars@engineering.ucsb.edu
Dr. W. B. Im
School of Materials Science and Engineering
Chonnam National University
Gwangju 500-757, Republic of Korea
N. George, Prof. B. F. Chmelka
Department of Chemical Engineering
University of California Santa Barbara
Santa Barbara, CA 93106 USA
E-mail: bradc@engineering.ucsb.edu
J. Kurzman, Dr. A. Mikhailovsky
Department of Chemistry and Biochemistry
University of California Santa Barbara
Santa Barbara, CA 93106 USA
S. Brinkley
Department of Electrical and Computer Engineering
University of California Santa Barbara
Santa Barbara, CA 93106 USA
Dr. J. Hu
Materials Research Laboratory
University of California Santa Barbara
Santa Barbara, CA 93106 USA

DOI: 10.1002/adma.201003640

SAF belongs to the Cs_3CoCl_5 structural family, (tetragonal, space group $I4/mcm$)[40] and is also closely related to $Sr_3M^{4+}O_5$-type compounds, including SSO (tetragonal, space group $P4/ncc$).[41] The SAF lattice is composed of $[Sr1_2F]^{3+}$ layers (zSr = 0) alternating with $[Sr_2AlO_4]^{3-}$ layers (zSr = zAl = 1/4) along the c-axis. SSO has alternating layers of $[Sr1_2O]^{2+}$ (z_{Sr1} = 1/4) and $[Sr_2SiO_4]^{2-}$ ($z_{Sr2} = z_{Si} = 0$). In the SAF unit cell, the AlO_4 tetrahedra are eclipsed with their upper and lower edges parallel to the face diagonal of the [001] plane. The SiO_4 tetrahedra in the SSO are staggered, which leads to the lower symmetry space group $P4/ncc$ of SSO instead of $I4/mcm$ for SAF.

Samples of SASF:Ce^{3+} were observed to crystallize as nearly single-phase compounds similar to the SAF or SSO structures as seen from the XRD patterns of SASF:Ce^{3+} (x = 0, 0.1, 0.3, 0.5, 0.7, 0.9, and 1.0) shown in **Figure 1**a. Alloying of Al^{3+}/Si^{4+} perturbs lattice perfection near the z = 1/4 and 3/4 layers for SAF and z = 0 and 1/2 layers for SSO; this is observed from the broadening of XRD [00l] reflections. For example, the [004] reflections have the full width at half-maximum (FWHM) values of 0.102, 0.189, 0.297, 0.290, 0.284, 0.192, and 0.106 for SASF:Ce^{3+} with x values of 0, 0.1, 0.3, 0.5, 0.7, 0.9, and 1.0, respectively. The increased FWHM for intermediate compositions x clearly indicates alloying of Al^{3+}/Si^{4+}. The sudden change between x = 0.7 and x = 0.9 of the reflection positions of the [004], [220], and [310] planes at 2θ angles of approximately 32°, 37.5°, and 42.5°, respectively, as well as the sudden changes of other reflection positions show that the phase change from SAF to SSO occurs in this range of compositions. The fact that the phase change occurs between x = 0.7 and x = 0.9 shows that SAF can withstand more strain and distortions than SSO.

XRD data were fit using the Rietveld method with the program GSAS (Figure S2, Supporting Information).[42] The SAF structure was used as the model for $x \leq 0.7$; the SSO structure was used for $x > 0.7$. The final weighted R factors (R_{wp}) of all samples successfully converged to satisfactory values (R_{wp} = 3.73% to 6.37%). Site disordering between F^- and O^{2-} was not considered since ^{19}F NMR results showed no evidence of this for all materials. The lattice parameters of pure SAF:Ce^{3+} (x = 0) were refined to be $a = b$ = 6.7720(1) Å, c = 11.1485(2) Å (numbers in parentheses indicate standard deviations in the last decimal place) and those of SSO:Ce^{3+} (x = 1.0) were refined to be $a = b$ = 6.9539(1) Å and c = 10.7657(3) Å with lattice parameters of intermediate compositions varying linearly (Figure S3, Supporting Information), obeying the Végard law. The increase of one parameter and the contraction of the other may arise from the replacement of the larger Al^{3+} cation (r_1 = 0.39 Å) by the smaller Si^{4+}(r_4 = 0.26 Å) taking place concurrently with replacement of the smaller F^- anion (r_6 = 1.33 Å) by the larger O^{2-} (r_6 = 1.40 Å).[43] Contraction of cell parameter c and expansion of a and b as x increases causes the Al/Si tetrahedra to stagger in the c-direction, as evident from the change in space group between x = 0.7 and x = 0.9. Changes in cell parameters and symmetry also cause greater distortion around the Sr polyhedra, which effects the optical properties, as discussed presently.

The environment of fluorine in SASF:Ce^{3+} are key to understanding the optical properties of the phosphors. Oxygen and fluorine are difficult to distinguish by diffraction techniques; O^{2-} and F^- have essentially no contrast in X-ray scattering and very little contrast in their coherent neutron scattering lengths.[44] However, solid-state ^{19}F NMR allows the environments of ^{19}F (100% natural abundance) to be probed in detail. Figure 1b shows single-pulse ^{19}F magic-angle spinning (MAS) NMR spectra for $Sr_{2.975}Ce_{0.025}Al_{1-x}Si_xO_{4+x}F_{1-x}$ with values of x ranging from 0 to 0.9, which yielded a single isotropic peak in the range of –101 to –113 ppm for each material. Linewidths ranged from 4–9 ppm FWHM (Figure S4, Supporting Information). As x increases, a shift to lower frequency and a decrease in the intensities of the ^{19}F peaks are observed.

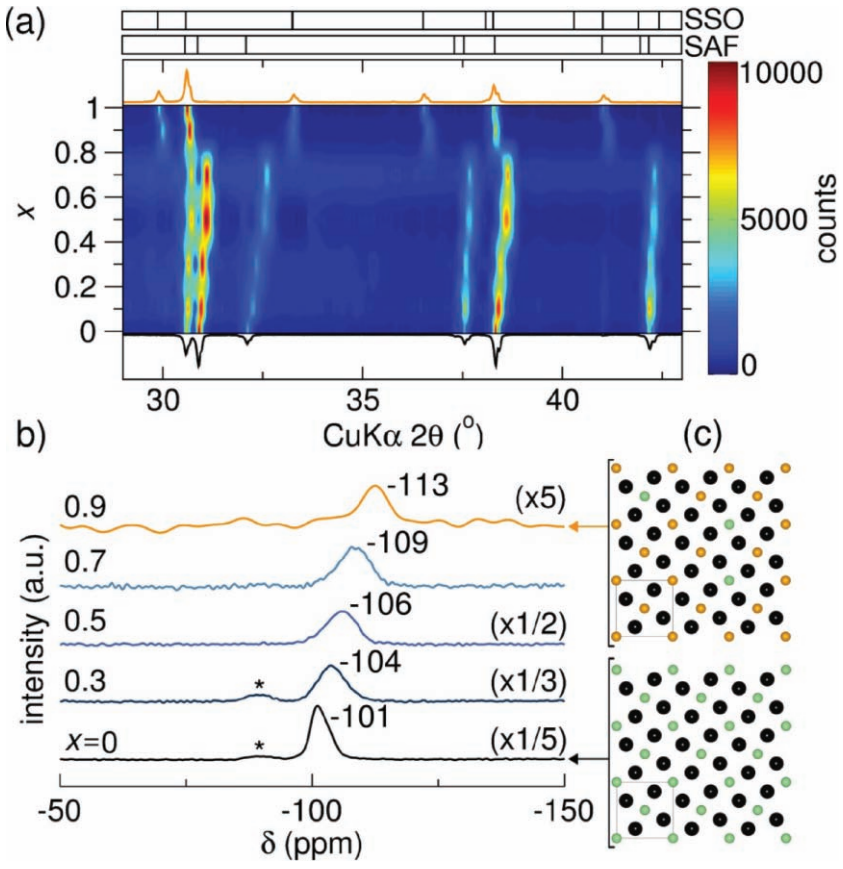

Figure 1. a) XRD patterns for $Sr_{2.975}Ce_{0.025}Al_{1-x}Si_xO_{4+x}F_{1-x}$ with x = 0, 0.1, 0.3, 0.5, 0.7, 0.9, and 1; b) solid-state ^{19} F MAS NMR spectra acquired under 60 kHz MAS at 300 K of SASF:Ce^{3+} solid solutions; and c) schemes of the [001] plane for materials with x = 0 (100% F, bottom) and x = 0.9 (10% F and 90% O, top). Expected reflection positions for the end-members are displayed on the top (a) and data for the end members are displayed above and below the center plot; the phase boundary is between x = 0.7 and x = 0.9. Some spectra in (b) have been multiplied by the factors indicated on the right. ^{19}F isotropic chemical shifts are referenced to a Teflon standard. The asterisks in (b) indicate an SrF_2 impurity. Green atoms in (c) are F and orange are O.

The single ^{19}F signals in each of the spectra indicate that the fluoride ions reside in a single crystallographic site regardless of the composition, *x*. Fluorine is known to be well-ordered in the SAF structure, as previously reported,[45,46] and the findings here from ^{19}F NMR support this. The reduction in the intensities of the ^{19}F signals as *x* increases reflects the relative reduction in the overall amount of ^{19}F in the materials. The displacement of the isotropic ^{19}F signals to lower frequencies with increasing *x* indicates greater shielding of the respective ^{19}F nuclei, suggesting an increase of the electron densities around the ^{19}F nuclei. This displacement is consistent with substitution of more electronegative F atoms by O atoms with increasing *x*. Alternatively, this can be thought of as $[Sr1_2O]^{2+}$ layers, which have a greater electron density, in the [001] plane replacing $[Sr1_2F]^{3+}$ layers. This suggests an increase in lattice covalency, which is consistent with red-shifts of the emission and excitation wavelengths of Ce^{3+} ions in the lattice.[57]

The high degree of crystallinity established by the XRD patterns in Figure 1a and single ^{19}F signals in Figure 1b are consistent with the ^{19}F nuclei residing in a single crystallographic site in the SASF:Ce^{3+} materials. However, the widths of the ^{19}F peaks indicate a distribution of local ^{19}F electronic environments in the materials. The ^{19}F FWHM increases modestly from ca. 4 ppm to ca. 9 ppm with increasing *x*, reflecting a broader range of local ^{19}F environments as *x* increases. The broader linewidths as ^{19}F atoms become more dilute are consistent with inhomogeneous broadening of signals from locally heterogeneous ^{19}F sites, with possible contributions from ^{19}F–^{19}F dipolar coupling, especially for high fluorine contents. Several of the ^{19}F peaks exhibit modest asymmetries, which may be due to non-uniform atomic substitutions of F or Si atoms, paramagnetic effects induced by Ce^{3+} species (previously observed for ^{119}Sn and ^{89}Y NMR signals in pyrochlores[47,48]), or perturbations in the lattice resulting from Ce^{3+} substituting for Sr^{2+} cations. Asterisks in Figure 1b correspond to ^{19}F signals from small amounts of impurities, notably SrF_2 at –89 ppm, which is only observed for materials with high fluorine contents ($x \leq 3$). SrF_2 is known to result from decomposition of the SASF:Ce^{3+} phosphor due to moisture. The ^{19}F NMR spectra show that the amount of SrF_2 decreases as *x* increases and no SrF_2 is detectable for $x > 0.3$. This shows that increasing SSO content in SASF:Ce^{3+} improves moisture stability.

Pair-distribution-function (PDF) analyses with synchrotron total scattering facilitate an understanding of the local structures in the SASF solid solution.[49] Although the solid-solution series obeys the Végard law, the actual local bond lengths and coordination environments can be different from those in average crystal structure models.[49,50] Details of the PDF analysis are presented in the Supporting Information and Figure S5. The key result is that the composition for $Sr_{2.975}Ce_{0.025}Al_{1-x}Si_xO_{4+x}F_{1-x}$ of $x = 0.5$, unlike other compositions, possesses a relatively large range of Sr1–O2 distances about 2.6 Å and Sr1–Al/Si distances centered ca. 3.2 Å. This is observed through the broadening of a peak at 2.6 Å and the absence of intensity (possibly due to broadening) about 3.2 Å for the $x = 0.5$ composition. This suggests a range of bonding environments permit the substituted Ce^{3+} ions to bond optimally in the $x = 0.5$ material.

Figure 2 shows photoluminescent (PL) excitation and emission spectra of $Sr_{2.975}Ce_{0.025}Al_{1-x}Si_xO_{4+x}F_{1-x}$ ($x = 0.0$, 0.1, 0.3, 0.5, 0.7, 0.9, and 1.0) and a commercial $Y_3Al_5O_{12}$:Ce^{3+} (YAG:Ce^{3+}) sample. The respective maxima in excitation/emission intensity were used to record the emission/excitation spectra. The solid solution has excellent phosphor properties with 390 nm, 400 nm, 430 nm, and 450 nm excitation; all of these wavelengths have been used as excitation sources from LED chips. Broad, largely green emission spectra are observed, arising from electronic transitions of Ce^{3+} from its 5d ($^2D_{3/2}$,$^2D_{5/2}$) excited state to the 4f ($^2F_{5/2}$,$^2F_{7/2}$) ground state.[51] With increasing SSO content *x*, the emission peak positions gradually move toward longer wavelengths, in the range from 474 nm for SAF:Ce^{3+} ($x = 0$) to 537 nm for SSO:Ce^{3+} ($x = 1.0$). This 63 nm shift allows highly color-tunable phosphors. It is interesting to note the non-monotonic increase of the excitation wavelength maximum with varying *x*, which is associated with a monotonic shift in the emission maximum wavelength. The solid-solution phosphors have wider emission peaks than SAF:Ce^{3+} (Table S2, Supporting Information), which allows SASF:Ce^{3+} phosphors to provide enhanced color rendering properties when incorporated into an LED chip.

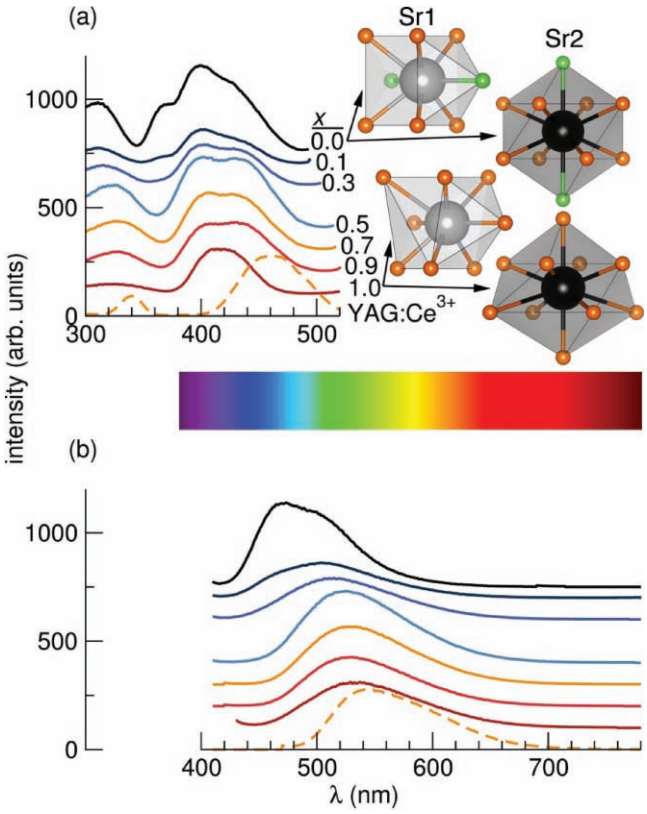

Figure 2. a) Excitation and b) emission spectra of the solid solution phosphors SASF:Ce^{3+} with the various *x* values indicated. For comparison, the excitation and emission spectra of a YAG:Ce^{3+} phosphor are also shown. Spectra have been offset for clarity. Sr1 and Sr2 polyhedra looking down the [100] direction are shown to the right of (a); the upper two polyhedra are from the SAF structure and the lower two are from the SSO structure. Light gray, black, orange, and green spheres represent Sr1, Sr2, O, and F atoms, respectively.

A conventional d-orbital splitting model predicts a blue-shift in the emission as *x* increases, based on the increasing

average Sr–O/F distance.[14,52] Although the average Sr–O/F bond length increases with increasing x (Figure S6, Supporting Information), the coordination around both Sr sites, shown in Figure 2a, becomes increasingly anisotropic as x increases. Red-shifted emission in garnets has been previously attributed to increasing distortion around the active site, which causes an increased crystal field splitting.[53] Therefore, the emission red-shift is partially attributed to increasing distortion of the active sites. The increasing covalency (nephelauxetic effect) in the lattice as x increases also contributes to a red-shift of the excitation and emission spectra.[54] This is supported by the work of Dorenbos, who systematically studied the position of the [Xe]5d ^{1} configuration of Ce^{3+} within various host lattices by using parameters such as anion polarizability and cation electronegativity. He found oxides tend to have a greater centroid shift of the d-orbitals than fluorides leading to an emission red-shift.[55–58] In garnet phosphors, distortions around the Ce^{3+} sites have been observed to shift the 5d ($^2D_{3/2}$,$^2D_{5/2}$) (emission) by a greater amount than the 4f ($^2F_{5/2}$,$^2F_{7/2}$) (excitation) energy levels.[53] The non-monotonic shift of excitation wavelength and monotonic shift of emission wavelength with x observed here is due to the changing crystal field around Ce^{3+} sites and the changing covalency of the lattice having different effects on the 5d ($^2D_{3/2}$,$^2D_{5/2}$) and 4f ($^2F_{5/2}$,$^2F_{7/2}$) energy levels.

The measured values of quantum efficiency in $Sr_{2.975}Ce_{0.025}Al_{1-x}Si_xO_{4+x}F_{1-x}$ were 83% for the $x = 0.0$ material and 85% for the $x = 0.5$ material at room temperature (Table S2, Supporting Information), close to that of commercial YAG:Ce^{3+}, which was determined to be 81%. $Sr_{2.975}Ce_{0.025}Al_{0.5}Si_{0.5}O_{4.5}F_{0.5}$ ($x = 0.5$), which has the symmetry of SAF, had the highest PL intensity (λ_{ex} = 430 or 450 nm) and highest quantum efficiency (85%) of all SASF:Ce^{3+} materials. This may be due to Ce^{3+} ions bonding optimally in the structure, which is supported by the PDF analyses.

Conversion efficiency of the phosphors declined as the LED operation temperature increased (Figure S8, Supporting Information) as a result of increased non-radiative transition probability in the configurational coordinate diagram.[14,51] As the temperature increased from 25°C to 170°C, the maximum PL intensity of the $x = 0.5$ phosphor decreased to 55% of the initial value. A commercial YAG:Ce^{3+} standard decreased to 64% of the initial PL intensity. Other SASF:Ce^{3+} compositions decreased more than the YAG:Ce^{3+} standard. The thermal quenching diminishes as the amount of fluorine decreases; this arises from softer phonon modes associated with fluorine atoms in the host. However, the SSO:Ce^{3+} ($x = 1.0$) phosphor had improved thermal quenching properties compared to the $x = 0.7$ or $x = 0.9$ materials. Disordering of Al^{3+}/Si^{4+} and $F^-/Ol^{â^,2}$ provides an alternate quenching path in the host lattice which outweighs the softer phonon modes of F, thereby reducing efficiency.

Each factor that contributes to efficiency must be optimized to achieve the highest possible luminous efficacy in a phosphor-converted LED (pcLED). Package efficiency in white LEDs is typically around 40% and 60%.[59] Loss in pcLEDs is partly associated with reflection of the incident light source and emitted yellow light back towards the chip. To reduce this loss, we have produced a new pcLED design, shown in **Figure 3**, which has a small air gap ($n = 1$) between the epoxy on the LED chip ($n \approx 1.5$) and the phosphor cap ($n \approx 1.7$) that can reduce the amount of light reflected back into the chip, due to the differences in refractive indices of the various layers. Also, the phosphor layer is insulated from the heat generated by the LED chip, reducing thermal quenching effects. Using this new structure increases the value of luminous efficacy by nearly a factor of two when compared with our previous study on the $x = 1.0$ end-member.[38]

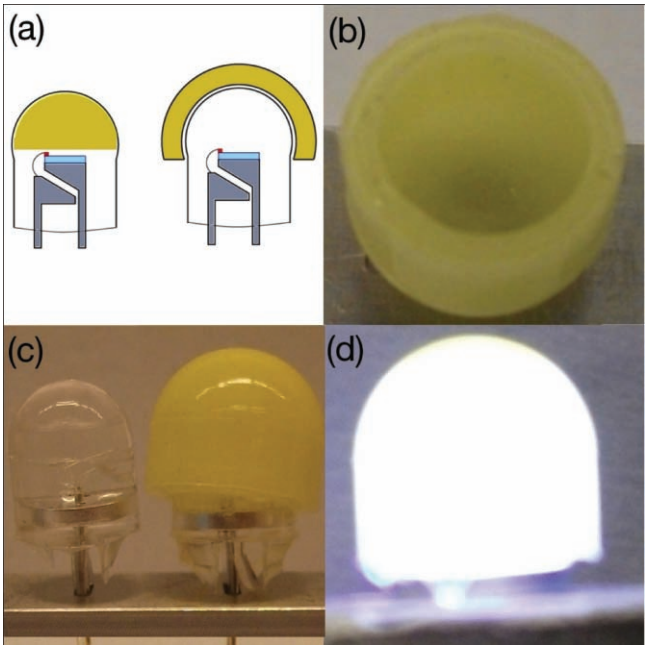

Figure 3. a) Schemes of LEDs with phosphor particles in the encapsulant (left) and with phosphor particles molded with encapsulant into a cap that is placed on top of the LED (right). b) Photograph of a phosphor cap molded with silicone resin. c) Conventional LED without phosphor (left, ca. 8 mm diameter) and the LED with a phosphor cap (right, ca. 12 mm diameter). d) Image of a phosphor-capped LED under 20 mA forward bias.

Incorporating the $x = 0.5$ $Sr_{2.975}Ce_{0.025}Al_{1-x}Si_xO_{4+x}F_{1-x}$ phosphor into a device allows comparison of the performance with a device made with commercial YAG:Ce^{3+} phosphors. **Figure 4**a shows the electroluminescence (EL) spectra acquired for $x = 0.5$ SASF:Ce^{3+} material integrated into a device with an InGaN LED (λ_{max} = 434 nm) under a 20 mA forward bias current. Broad EL is observed in the range of 500–600 nm and the device was established to have an efficacy of 73 lm W^{-1}, R_a = 69 and a CCT of 6937 K. The emission peak width (and hence color rendering) can be increased by adding a proprietary red phosphor to the silicone resin in the amounts 15 wt% SASF:Ce^{3+} and 3 wt% red phosphor to the device; the EL spectra for the device with the $x = 0.5$ SASF:Ce^{3+} and a proprietary red phosphor is shown in Figure 4a. The Commission Internationale de l'Eclairage (CIE) coordinates of the devices lie near the Planckian locus, shown in Figure 4b. Adding the red phosphor has the effect of increasing R_a to 81 with a CCT of 4371 K, although efficacy is reduced to 61 lm W^{-1}. White LEDs based on commercial YAG:Ce^{3+} phosphors fabricated using the same conditions as that of SASF:Ce^{3+} had a higher value of efficacy (91 lm W^{-1}) than SASF:Ce^{3+} (73 lm W^{-1}), despite the high

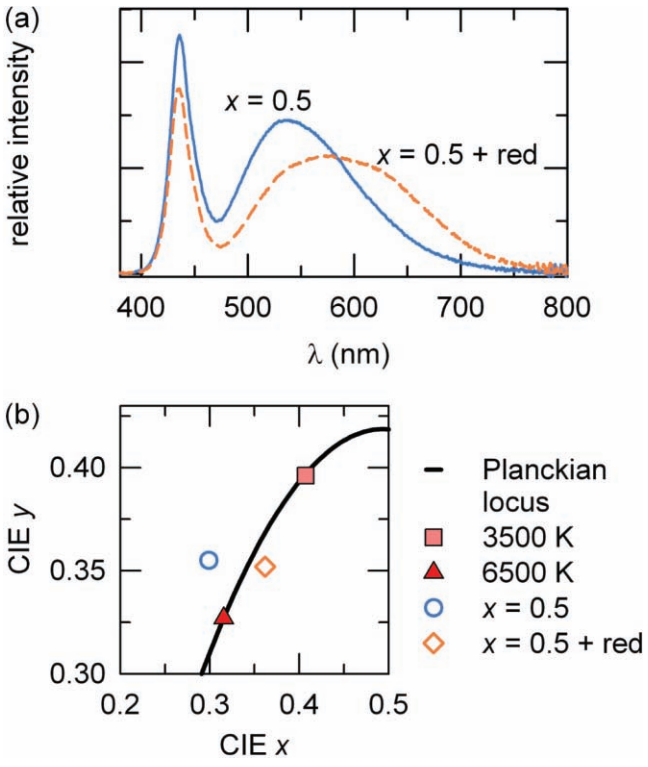

Figure4. a) Electroluminescence spectra of the $Sr_{2.975}Ce_{0.025}Al_{1-x}Si_xO_{4+x}F_{1-x}$ phosphor (x = 0.5) with (dashed) and without (solid) a red phosphor incorporated into an InGaN LED (λ_{max} = 434 nm) under 20 mA forward bias current and b) CIE chromaticity coordinates of the device. The Planckian locus line and the points corresponding to color temperatures of 3500 K and 6500 K are indicated in (b).

QE of the x = 0.5 SASF:Ce^{3+} phosphor. However, the YAG:Ce^{3+} LED had worse color rendering, with R_a = 64 and a CCT of 4011 K. It is anticipated that all properties in this system can be further improved with further optimization of factors such as phosphor particle size.

In conclusion, we have developed new green-yellow-emitting phosphors by making solid solutions of varying compositions between Sr_3AlO_4F and Sr_3SiO_5 phosphor hosts. $Sr_{2.975}Ce_{0.025}Al_{1-x}Si_xO_{4+x}F_{1-x}$ (SASF:Ce^{3+}) phosphors have high values of QE and high tunability in excitation and emission energy. By adopting a phosphor-capped layer with an air gap between the epoxy layer on the LED chip, we obtained white LEDs with a efficacy of 73 lm W^{-1} under 20 mA forward bias, with an R_a = 69 and CCT of 6937 K. This newly developed solid solution phosphor shows great potential for use in white LEDs, due to its high luminous efficacy, as well as tunability in excitation and emission.

Experimental Section

Powder samples of $Sr_{2.975}Ce_{0.025}Al_{1-x}Si_xO_{4+x}F_{1-x}$ (SASF:Ce^{3+}, x = 0, 0.1, 0.3, 0.5, 0.7, 0.9, and 1.0) were prepared by solid-state reaction starting from $SrCO_3$ (Aldrich, 99.995%), SrF_2 (Aldrich, 99.9%), Al_2O_3 (Aldrich, 99.9%), SiO_2 (Johnson Matthey, 99.9%), and CeO_2 (Aldrich, 99.9%). The powder reagents were intimately ground together with acetone in an agate mortar, placed in high purity alumina crucibles, and heated between 1200 °C and 1400 °C in a H_2:N_2 (5%:95%) atmosphere for 4 h. After heat treatment, the samples were gradually cooled to room temperature inside the furnace. The phosphor cakes were then ground into fine powders. Phosphor-converted solid-state lighting devices were constructed around discrete LEDs grown on *m*-plane GaN,[60] which were placed on silver headers with gold wires attached for electrical operation. The LEDs emit with λ_{max} = 434 nm. Intimate mixtures of SASF:Ce^{3+} (x = 0.5) and transparent silicone resin were then either directly placed and cured on the LED chip or molded as caps that fit on top of a clear silicone-capped LED. After packaging was completed, the optical properties of the device were measured in an integrating sphere under forward DC bias conditions. Details of other characterization techniques can be found in the Supporting Information.

Supporting Information

Supporting Information is available from the Wiley Online Library or from the author.

Acknowledgements

The authors thank Claude Weisbuch and Ramzy Shayib for discussions; Serena Corr, Peter Chupas, and Karena Chapman for assistance with synchrotron data collection; and Karun Vijayraghavan for assistance with the fabrication of the white LEDs. This work was partially supported by the MRSEC Program of the National Science Foundation under Award No. DMR05-20415, also acknowledged for the use of the facilities of the NSF-funded Materials Research Facilities Network (www.mrfn.org). Use of the Advanced Photon Source at Argonne was supported by the U. S. Department of Energy, Office of Science, Office of Basic Energy Sciences, under Contract No. DE-AC02-06CH11357. This article is part of the Special Issue on Materials Research at the University of California, Santa Barbara.

Received: October 5, 2010
Published online: April 8, 2011

[1] S. Pimputkar, J. S. Speck, S. P. DenBaars, S. Nakamura, *Nat. Photonics* **2009**, *3*, 180.
[2] E. F. Schubert, J. K. Kim, *Science* **2005**, *308*, 1274.
[3] T. Hashimoto, F. Wu, J. S. Speck, S. Nakamura, *Nat. Mater.* **2007**, *6*, 568.
[4] S. Nakamura, *MRS Bull.* **2009**, *34*, 101.
[5] B.-H. Kim, C.-H. Cho, J.-S. Mun, M.-K. Kwon, T.-Y. Park, J. S. Kim, C. C. Byeon, J. Lee, S.-J. Park, *Adv. Mater.* **2008**, *20*, 3100.
[6] H. S. Jang, H. Yang, S. W. Kim, J. Y. Han, S.-G. Lee, D. Y. Jeon, *Adv. Mater.* **2008**, *20*, 2696.
[7] J. Lim, S. Jun, E. Jang, H. Baik, H. Kim, J. Cho, *Adv. Mater.* **2007**, *19*, 1927.
[8] J. Ziegler, S. Xu, E. Kucur, F. Meister, M. Batenschuk, F. Gindele, T. Nann, *Adv. Mater.* **2008**, *20*, 4068.
[9] J. Lee, V. C. Sundar, J. R. Heine, M. G. Bawendi, K. F. Jensen, *Adv. Mater.* **2000**, *12*, 1102.
[10] E. F. Schubert, *Light-emitting diodes*, 2nd edition, Cambridge **2006**.
[11] W. B. Im, S. Brinkley, J. Hu, A. Mikhailovsky, S. P. DenBaars, R. Seshadri, *Chem. Mater.* **2010**, *22*, 2842.
[12] G. Blasse, W. L. Wanmaker, J. W. ter Vrugt, A. Bril, *Philips Res. Repts.* **1968**, *23*, 189.
[13] J. K. Park, C. H. Kim, S. H. Park, H. D. Park, S. Y. Choi, *Appl. Phys. Lett.* **2004**, *84*, 1647.
[14] S. Shionoya, W. M. Yen, *Phosphor Handbook*, CRC Press, New York **1998**.
[15] C. Feldmann, T. Justel, C. R. Ronda, P. J. Schmidt, *Adv. Funct. Mater.* **2003**, *13*, 511.

[16] Y. Shimomura, T. Kurushima, N. Kijima, *J. Electrochem. Soc.* **2007**, *154*, J234.
[17] Y. Shimomura, T. Honma, M. Shigeiwa, T. Akai, K. Okamoto, N. Kijima, *J. Electrochem. Soc.* **2007**, *154*, J35.
[18] A. A. Setlur, W. J. Heward, Y. Gao, A. M. Srivastava, R. G. Chandran, M. V. Shankar, *Chem. Mater.* **2006**, *18*, 3314.
[19] A. A. Setlur, W. J. Heward, M. E. Hannah, U. Happek, *Chem. Mater.* **2008**, *20*, 6277.
[20] M. H. Kostova, C. Zollfrank, M. Batentschuk, F. Goetz-Neunhoeffer, A. Winnacker, P. Greil, *Adv. Funct. Mater.* **2009**, *19*, 599.
[21] Y. C. Kang, H. S. Roh, S. B. Park, *Adv. Mater.* **2000**, *12*, 451.
[22] A. A. Setlur, E. V. Radkov, C. S. Henderson, J.-H. Her, A. M. Srivastava, N. Karkada, M. S. Kishore, N. P. Kumar, D. Aesram, A. Deshpande, B. Kolodin, L. S. Grigorov, U. Happek, *Chem. Mater.* **2010**, *22*, 4076.
[23] W. Chen, H. Liang, B. Han, J. Zhong, Q. Su, *J. Phys. Chem.* **2009**, *113*, 17194.
[24] V. Bachmann, C. Ronda, O. Oeckler, W. Schnick, *Chem. Mater.* **2009**, *21*, 316.
[25] J. A. Kechele, C. Hecht, O. Oeckler, J. S. auf der Günne, P. J. Schmidt, W. Schnick, *Chem. Mater.* **2009**, *21*, 1288.
[26] C. Hecht, F. Stadler, P. J. Schmidt, J. S. auf der Günne, V. Baumann, W. Schnick, *Chem. Mater.* **2009**, *21*, 1595.
[27] M. Zeuner, P. J. Schmidt, W. Schnick, *Chem. Mater.* **2009**, *21*, 2467.
[28] Y. Q. Li, A. C. A. Delsing, G. de With, H. T. Hintzen, *Chem. Mater.* **2005**, *17*, 3242.
[29] R. J. Xie, N. Hirosaki, K. Sakuma, Y. Yamamoto, M. Mitomo, *Appl. Phys. Lett.* **2004**, *84*, 5404.
[30] T. Suehiro, N. Hirosaki, R. J. Xie, M. Mitomo, *Chem. Mater.* **2005**, *17*, 308.
[31] H. S. Yoo, W. B. Im, S. Vaidyanathan, B. J. Park, D. Y. Jeon, *J. Electrochem. Soc.* **2008**, *155*, J66.
[32] Y. S. Hu, W. D. Zhuang, H. Q. Ye, S. S. Zhang, Y. Fang, X. W. Huang, *J. Lumin.* **2005**, *111*, 139.
[33] Q. H. Zhang, J. Wang, R. J. Yu, M. Zhang, Q. Su, *Electrochem. Solid State Lett.* **2008**, *11*, H335H.
[34] J. Liu, H. Z. Lian, C. S. Shi, J. Y. Sun, *J. Electrochem. Soc.* **2005**, *152*, G880.
[35] H. S. Jang, W. B. Im, D. C. Lee, D. Y. Jeon, S. S. Kim, *J. Lumin.* **2007**, *126*, 371.
[36] M. Nyman, L. E. Shea-Rohwer, J. E. Martin, P. Provencio, *Chem. Mater.* **2009**, *21*, 1536.
[37] W. B. Im, N. N. Fellows, S. P. DenBaars, R. Seshadri, Y.-I. Kim, *Chem. Mater.* **2009**, *21*, 2957.
[38] W. B. Im, N. N. Fellows, S. P. DenBaars, R. Seshadri, *J. Mater. Chem.* **2009**, *19*, 1325.
[39] W. B. Im, Y. Fourré, S. Brinkley, J. Sonoda, S. Nakamura, S. P. DenBaars, R. Seshadri, *Opt. Express* **2009**, *17*, 22673.
[40] M. Drofenik, L. Golic, *Acta Crystallogr.* **1979**, *B35*, 1059.
[41] L. S. Dent, F. P. Glasser, *Acta Crystallogr.* **1965**, *18*, 453.
[42] A. C. Larson, R. B. Von Dreele, *Los Alamos National Laboratory Report LAUR 86-748*, Los Alamos National Laboratory, Los Alamos **2004**.
[43] R. D. Shannon, *Acta Crystallogr.* **1976**, *A32*, 751.
[44] L.-S. Du, A. Samoson, T. Tuherm, C. P. Grey, *Chem. Mater.* **2000**, *12*, 3611.
[45] T. Vogt, P. M. Woodward, B. A. Hunter, A. K. Prodjosantoso, B. J. Kennedy, *J. Solid State Chem.* **1999**, *144*, 228.
[46] A. K. Prodjosantoso, B. J. Kennedy, T. Vogt, P. M. Woodward, *J. Solid State Chem.* **2003**, *172*, 89.
[47] A. K. Cheetham, C. M. Dobson, C. P. Grey, R. J. B. Jakeman, *Nature* **1987**, *328*, 706.
[48] C. P. Grey, M. E. Smith, A. K. Cheetham, C. M. Dobson, R. Dupree, *J. Am. Chem. Soc.* **1990**, *112*, 4760.
[49] a) T. Egami, S. J. L. Billinge, *Underneath the Bragg peaks: structural analysis of complex materials*, Pergamon, Amsterdam **2003**; b) T. Egami, *Ann. Rev. Mater. Res.*, **2007**, *37*, 297.
[50] I. K. Jeong, F. Mohiuddin-Jacobs, V. Petkov, S. J. L. Billinge, S. Kycia, *Phys. Rev. B* **2001**, *63*, 252021.
[51] G. Blasse, B. C. Grabmaier, *Luminescent materials*, Springer-Verlag, Berlin **1994**.
[52] P. D. Rack, P. H. Holloway, *Mater. Sci. Eng., R* **1998**, *21*, 171.
[53] J. L. Wu, G. Gundiah, A. K. Cheetham, *Chem. Phys. Lett.* **2007**, *441*, 250.
[54] C. K. Jörgensen, *Modern Aspects of Ligand Field Theory*, North-Holland, Amsterdam **1971**.
[55] P. Dorenbos, *Phys. Rev. B* **2000**, *62*, 15640.
[56] P. Dorenbos, *Phys. Rev. B* **2001**, *64*, 125117.
[57] P. Dorenbos, *Phys. Rev. B* **2002**, *65*, 235110.
[58] P. Dorenbos, *J. Lumin.* **2003**, *105*, 117.
[59] S. C. Allen, A. J. Steckl, *Appl. Phys. Lett.* **2008**, *92*, 1433091.
[60] M. C. Schmidt, K. C. Kim, H. Sato, N. Fellows, H. Masui, S. Nakamura, S. P. DenBaars, J. S. Speck, *Jpn. J. Appl. Phys.* **2007**, *46*, L126.

ADVANCED MATERIALS

Supporting Information

for Adv. Mater., DOI: 10.1002/adma.201003640

Efficient and Color-Tunable Oxyfluoride Solid Solution Phosphors for Solid-State White Lighting

Won Bin Im, Nathan George, Joshua Kurzman, Stuart Brinkley, Alexander Mikhailovsky, Jerry Hu, Bradley F. Chmelka,* Steven P. DenBaars,* and Ram Seshadri*

Supporting Information

Efficient and color-tunable oxyfluoride solid solution phosphors for solid-state white lighting

Won Bin Im,[a] *Nathan George,*[b,c] *Joshua Kurzman,*[d] *Stuart Brinkley,*[e,f] *Alexander Mikhailovsky,*[d] *Jerry Hu,*[b] *Bradley F. Chmelka,*[c] *Steven P. DenBaars,*[e,g] *and Ram Seshadri*[b,d,e,g]

[a]School of Materials Science and Engineering, Chonnam National University Gwangju 500-757, Republic of Korea
[b]Materials Research Laboratory, [c]Department of Chemical Engineering, [d]Department of Chemistry and Biochemistry, [e]Solid State Lighting and Energy Center, [f]Department of Electrical and Computer Engineering, and [g]Materials Department, University of California, Santa Barbara, CA 93106

Experimental Section

X-ray diffraction and synchrotron X-ray total scattering Powder X-ray diffraction (XRD) data were obtained using Cu-$K\alpha$ radiation (Philips X'Pert) over the angular range $20^\circ \leq 2\theta \leq 100^\circ$ with a step size of 0.016°. Crystal structure Rietveld refinements were performed using the General Structure Analysis System (GSAS) software suite.[1] Synchrotron X-ray total scattering data were collected in transmission mode on beamline 11-ID-B of the Advanced Photon Source, Argonne National Laboratory, at room temperature. Powder samples were loaded into Kapton™ tubes, sealed with glass wool and placed vertically in a sample holder in the path of the beam. Scattering data were collected with an image plate system (MAR345) and sample-to-detector distances of 305 mm using high energy X-rays ($\sim$90 keV). The use of high energy X-rays enables higher values of the wave vector, Q, which is critical for PDF extraction. Data for PDF analysis were collected in three exposures of 10 s to 60 s. The image-plate data were processed using the program FIT2D.[2] A ceria standard was used to calibrate the scattering.

Solid-state ^{19}F NMR Solid-state ^{19}F NMR spectroscopy was used to characterize the molecular compositions and structures of the solid solution phosphor compounds. The NMR experiments were carried out under conditions of magic angle spinning (MAS) at 300 K on a Bruker AVANCE IPSO NMR spectrometer, with an 11.7 T wide-bore superconducting magnet, operating at frequencies of 500.24 MHz for ^{1}H and 470.39 MHz for ^{19}F. A Bruker 1.3 mm H-X double-resonance MAS probe head was used with zirconia rotors and Kel-F® caps. A MAS spinning rate of 60 kHz was used to reduce effects from ^{19}F-^{19}F dipolar coupling interactions. Chemical shifts were referenced to Teflon™, which was assigned a chemical shift of -122 ppm relative to a shift of 0 ppm for $CFCl_3$.

A total of 32 1D single-pulse ^{19}F spectra were recorded using a $30\,^{\circ}$ pulse length of 1.7 μs and a recycle delay of 150 s.

Optical properties: PL, quantum efficiency, temperature-dependent PL, and fluorescence lifetime PL spectra were measured on a Perkin Elmer LS55 luminescence spectrophotometer scanning the wavelength range of 300 nm to 800 nm at room temperature (RT). Photoluminescence quantum efficiency in solid samples was determined by a method derived from that reported by Greenham *et al.* [3] Phosphor powders encapsulated in silicone resin (GE Silicones, RTV615) were deposited on transparent quartz substrates (Chemglass) with dimensions of 12×12 mm. These substrates were then placed in a Spectralon™-coated integrating sphere (6 inch diameter, Labsphere) at an angle slightly different from normal incidence to avoid back reflection of the laser beam. An Ar^{+}–laser (Spectraphysics Beamlock 2065) was used for generation of light with wavelength 457 nm. 405 nm light was produced by a solid-state laser (Crystalaser). The laser power used in experiments was between 1 and 2 mW. The light exciting the integrating sphere was collected by a quartz lens and directed onto a calibrated Si photodiode (Newport 818-UV). Bandpass or long wavelength-pass interference filters (Omega Filters) were inserted in front of the detector to measure laser light and PL intensities, respectively. The laser beam was modulated by a chopper (SRS SR540) and a lock-in amplifier (SRS SR830) was used to measure the detector's photocurrent. Data collection and processing procedures were similar to those described by Greenham, *et al.* [3] with adjustments for opaque samples. Temperature quenching characteristics were measured using a home-built fluorimeter incorporating a heating stage (Instec) allowing heating of the sample up to 443 K.

Fluorescence lifetime measurements were performed using the time-correlated single photon counting (TCSPC) technique. [4] Approximately 100 femtosecond (fs) excitation pulses with wavelength 405 nm were generated by doubling the fundamental frequency of a Ti:sapphire laser (Spectraphysics Tsunami) pulses in β-barium borate crystal. The laser repetition rate was reduced to 200 KHz by a home-made acousto-optical pulse picker to avoid saturation of the chromophore. The TCSPC system was equipped with an ultrafast microchannel plate photomultiplier tube detector (Hamamatsu R3809U-51) and electronics board (Becker & Hickl SPC-630) and had an instrument response time between 60 and 65 ps. The triggering signal for the TCSPC board was generated by sending a small fraction of the laser beam onto a fast (400 MHz bandwidth) Si photodiode (Thorlabs Inc.). The fluorescence signal was dispersed in an Acton Research SPC-300 monochromator after passing through a pump-blocking, long wavelength-pass, autofluorescence-free interference filter (Omega Filters, ALP series). The monochromator was equipped with a CCD camera (Roper Scientific PIXIS-400) allowing for monitoring of the time-averaged fluorescence spectrum. Fluorescence transients were not deconvoluted with the instrument response function, since their characteristic time-constants were much longer than the width of the system response to the excitation pulse.

Discussion

PDF Analysis Pair-distribution-function (PDF) analyses with synchrotron total scattering facilitate an understanding of the local structures in the SASF solid solution.[5] Although the compounds follow the Végard law over the whole range of the solid solution, the actual local bond lengths and coordination environments can be different from those represented by average crystal structure models.[5,6] We find the PDFs of the end members Sr_3SiO_5 and Sr_3AlO_4F to be well described by the respective average structures. The addition of Si^{4+} and O^{2-} elements into the Sr_3AlO_4F host lattice manifests changes in the local structure of $Sr_{2.975}Ce_{0.025}Al_{1-x}Si_xO_{4+x}F_{1-x}$, as shown with the $x = 0.5$ sample in Figure S5b. The PDF of the $x = 0.5$ sample is not well modeled at low r by the $I4/mcm$ model that describes the average structure. At higher r, where there are more pairing contributions to $G(r)$, compositional mixing effects are less evident, and the average model agrees reasonably well with the medium range structure of SASF. The first peak in the experimental PDF centered about 1.7 Å is broadened (which corresponds mainly to Si–O/Al–O bonds). However, the model predicts a narrower distribution for this atom-atom distance due to symmetry constraints of the space-group which only allows for a single Si/Al–O distance. Given that a Si–O bond should be shorter than an Al–O bond, which arise at 1.68 Å and 1.78 Å in the respective end member refinements, the broadening of the peak around 1.6 Å in the PDF of SASF is not surprising. The largest discrepancy in the low r region is found near 3.2 Å, where there is calculated intensity not observed in the experimental $G(r)$; this peak corresponds mainly to a Sr1–Al/Si distance. This is most likely due to a higher amount of local disordering and possibly distortion effects that are present in the $x = 0.5$ sample, which may be due to the different Al–O and Si–O bond lengths in the structure (partially resulting from the difference in size between Al and Si). It is also possible that the peak which is observed in both end-member groups at 3.2 Å is overlapping with the large peak around 3.6 Å.

As the solid solution composition increases up to $x = 0.7$, the experimental values for $G(r)$ show a single peak in the range of 6.5 Å and 7.2 Å. This peak splits into two peaks for $x > 0.7$, highlighted on the far right of Figure S5(a). Analysis of the partial pairing contributions to the end-member (SSO and SAF) PDFs suggests this splitting is most likely due to an increase of a Sr1-Sr1 distance in the [001] plane from approximately 6.6 to 7 Å. This appears to be manifested as a nearly linear increase in the peak at 6.6 Å for $x = 0$ to the peak at 6.9-7 Å for $x = 1$. This peak splitting is the only largely obvious change from $x = 0.7$ to $x = 0.9$, which is where XRD results indicate a change in crystalline symmetry (Figure 1b). The PDF profile of the $x = 0.5$ sample showed significant differences at short lengths up to 3.5 Å. The peak centered around 2.6 Å, highlighted in Figure S5(a), shows a broader profile than for all other values of x, indicating a greater distribution of the Sr1–O2 bond distance that mainly contributes to this peak. This may be in part due to the greatly different Shannon-Prewitt ionic radii of 4-coordinated Si and Al, which are 0.26 Å and 0.39 Å, respectively.

Interatomic Distances and Crystal Field Splitting The distances between Sr and O/F atoms ($d_{\mathrm{Sr-O/F}}$) in the average structures for each Sr site are summarized from Rietveld refinement re-

sults in Figure S6. With increasing x in $Sr_{2.975}Ce_{0.025}Al_{1-x}Si_xO_{4+x}F_{1-x}$, the mean distances of $< d_{Sr-O/F} >$ for each Sr site linearly increased up to $x = 0.7$. We note that direct comparisons between materials with $x > 0.7$ and $x < 0.7$ are difficult, because the SASF:Ce^{3+} materials with $x = 0.9$ and 1.0 crystallize in the SSO structure. An interesting finding is that the mean d_{Sr1-O2} (x2) and $d_{Sr1-F/O1}$ distances at the 8h site in SASF:Ce^{3+} for the materials with $x = 0.5$ and $x = 0.7$ showed deviations from the linear trend of $< d_{Sr1-O/F} >$. The $d_{Sr1-F/O1}$ distance increased linearly with x until $x = 0.5$ where it leveled out *ca.* 2.5 Å. The values of $d_{Sr2-O/F}$ at the 4a site, however, linearly increased or decreased with x, suggesting that compositional mixing by Al^{3+}/Si^{4+} and F^-/O^{-2} strongly influence the local environments of Sr1 polyhedra unlike the Sr2 polyhedra. This might be due to $Sr_1O_6F_2$ polyhedra having more edge and corner sharing (two edges and two corners with (Al/Si)O_4 tetrahedra) than $Sr2O_8F_2$, which shares only two corners. Secondly, as a consequence of oxygen substitution for fluorine with increasing x, the $Sr1O_6F_2$ polyhedra have two different $d_{Sr1-O/F}$ distances. The oxygen at $4a$ site in the $Sr2O_8F_2$ polyhedra only contributes to the $d_{Sr2-F/O1}$, with intrinsically rigid AlO_4 tetrahedra in the $SrAlO_4$ layer.

The relation between the emission energy and the mean Sr–O/F distance in the SASF:Ce^{3+} compounds (not making assumptions with regard to which Sr in the structure is substituted by Ce^{3+}) is usually a function of the distance from Sr to its ligands. The d-orbital splitting of a metal center using a point charge model is given as [7,8]

$$Dq = \frac{Ze^2r^4}{6R^5}, \tag{S1}$$

where Dq corresponds to the energy level separation, Z is the valence of the anion ligand, e is electron charge, r is the radius of the frontier d wavefunction, and R is the distance between metal center and ligand. According to the above formula with an increase in $< d_{Sr-O/F} >$ with increasing x, one may expect a decreased crystal field splitting and hence a blue shift of emission wavelengths. However, this is not the case. Therefore, a crystal field analysis based on average Ce–ligand distances does not accurately represent the actual physical situation.

Decay Time Measurements Luminescence decay profiles of materials in the solid solution series recorded at room temperature are displayed in Figure S7, and can be fitted to an exponential function [9,7]

$$I = I_0 \exp(\frac{-t}{\tau_D}), \tag{S2}$$

where I_0 is the initial emission intensity for $t = 0$, and τ_D is lifetime. The excitation spectra suggest Ce^{3+} ions occupy both Sr sites. [10] All decay profiles can be fitted to single exponential functions, which suggests only one type of emitter (Ce^{3+}) is present. This also suggests that the decay kinetics of Ce^{3+} in both sites are very similar. Throughout the solid solution series, the luminescence decay displays similar exponential decay and similar decay times. The values of τ_D are fitted to be 39, 44, 56, 59, 51, and 50 ns for the different $Sr_{2.975}Ce_{0.025}Al_{1-x}Si_xO_{4+x}F_{1-x}$ materials. The decay time

of the luminescence increased as x increased up to 0.5, following which the decay time gradually decreased and plateaued.

^{19}F NMR The appearance of ^{19}F signals at lower frequencies may also be due to the Sr2–F distance orthogonal to the [001] plane decreasing linearly with increasing x as observed from Rietveld fitting of XRD (Figure S2). However, the Sr2–F distance only changes by 3.6% from $x = 0$ to 1 (Figure S6); therefore, the effect of substituting O atoms for F atoms with increasing x appears to dominantly effect the local electronic environment of the ^{19}F nuclei.

References

[1] A. C. Larson, R. B. Von Dreele, *Los Alamos National Laboratory Report LAUR 86-748*, Los Alamos National Laboratory, Los Alamos, **2004**.

[2] A. P. Hammersley, S. O. Svensson, M. Hanfland, A. N. Fitch, D. Hausermann, *Int. J. High Pressure Res.*, **1996**, *14*, 235-248.

[3] N. C. Greenham, I. D. W. Samuel, G. R. Hayes, R. T. Phillips, Y. A. R. R. Kessener, S. C. Moratti, A. B. Holmes, R. H. Friend, *Chem. Phys. Lett.*, **1995**, *241*, 89-96.

[4] W. Becker, *Advanced time-correlated single-photon counting techniques*, Springer, Berlin, New York, **2005**.

[5] T. Egami, S. J. L. Billinge, *Underneath the Bragg peaks: structural analysis of complex materials*, Pergamon, Amsterdam, Boston, **2003**; T. Egami, *Ann. Rev. Mater. Res.*, **2007**, *37*, 297.

[6] I. K. Jeong, F. Mohiuddin-Jacobs, V. Petkov, S. J. L. Billinge, S. Kycia, *Phys. Rev. B*, **2001**, *63*, 252021-252029.

[7] S. Shionoya, W. M. Yen, *Phosphor Handbook*, CRC Press, New York, **1998**.

[8] P. D. Rack, P. H. Holloway, *Mater. Sci. Eng., R*, **1998**, *21*, 171-219.

[9] G. Blasse, B. C. Grabmaier, *Luminescent materials*, Springer-Verlag, Berlin, New York, **1994**.

[10] W. B. Im, S. Brinkley, J. Hu, A. Mikhailovsky, S. P. DenBaars, R. Seshadri, *Chem. Mater.*, **2010**, *22*, 2842-2849.

Table S1: Structural parameters and select bond lengths (number of bonds in parentheses) in $Sr_{2.975}Ce_{0.025}Al_{0.5}Si_{0.5}O_{4.5}F_{0.5}$ (x = 0.5) as determined by the Rietveld refinement of powder XRD data at room temperature. Space group: $I4/mcm$ (No. 140), Z = 4, $a = b$ = 6.8417(1) Å, c = 10.9551(7) Å, V = 512.8(1) Å^3.

Atom	site	g	x	y	z
Sr1	$8h$	1.0	0.1773(5)	$x + \frac{1}{2}$	0
Sr2	$4a$	1.0	0	0	$\frac{1}{4}$
Al	$4b$	0.5	0	$\frac{1}{2}$	$\frac{1}{4}$
Si	$4b$	0.5	0	$\frac{1}{2}$	$\frac{1}{4}$
F	$4c$	0.5	0	0	0
O1	$4c$	0.5	0	0	0
O2	$16l$	1.0	0.1369(6)	$x + \frac{1}{2}$	0.6579(2)

Sr1–O2	(2×)	2.496(8) Å
	(4×)	2.774(7) Å
Sr1–F/O1	(2×)	2.519(5) Å
Sr2–O2	(8×)	2.839(4) Å
Sr2–F/O1	(2×)	2.738(5) Å

Table S2: Spectroscopic parameters associated with $Sr_{2.975}Ce_{0.025}Al_{1-x}Si_xO_{4+x}F_{1-x}$.

phosphor	excitation	emission	FWHM	Color chromaticity		QE
(x)	max. (nm)	max. (nm)	(nm)	CIE x	CIE y	(%)
0	400	474	98	0.168	0.291	83
0.1	400	503	106	0.233	0.417	22
0.3	402	516	108	0.284	0.485	46
0.5	433	525	105	0.317	0.536	85
0.7	406	527	106	0.333	0.548	70
0.9	430	530	105	0.332	0.547	67
1.0	420	537	113	0.342	0.522	62

Table S3: Optical properties of commercial YAG:Ce^{3+}, $Sr_{2.975}Ce_{0.025}Al_{1-x}Si_xO_{4+x}F_{1-x}$ (x = 0.5), and SASF:Ce^{3+} (x = 0.5) + red phosphor in white LEDs with a current of 20 mA.

phosphor	CCT	Efficacy	Color chromaticity		R_a
	(K)	(lm/W)	CIE x	CIE y	
YAG:Ce^{3+}	4011	91	0.393	0.428	64
x = 0.5	6937	73	0.299	0.355	69
x = 0.5 + red	4371	61	0.362	0.352	81

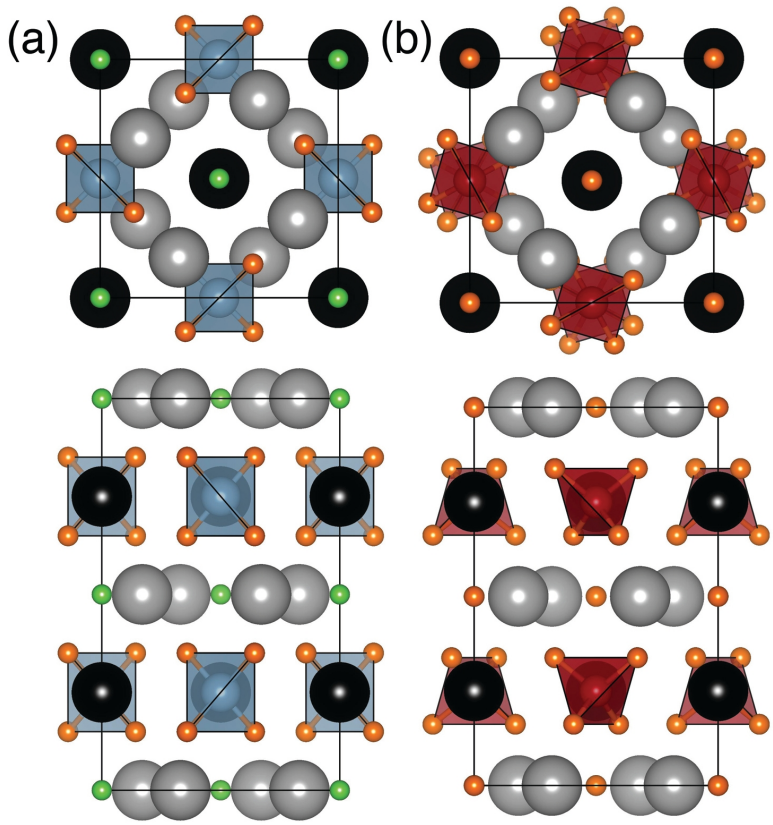

Figure S1: Projection of (a) Sr_3AlO_4F and (b) Sr_3SiO_5 structures down the [001] plane (top) and [100] plane (bottom). The origin of the SSO structure has been shifted by (0.5, 0, −0.25) for easier comparison with the SAF structure. Light gray, black, blue, red, orange, and green spheres represent Sr1, Sr2, Al, Si, O, and F atoms, respectively.

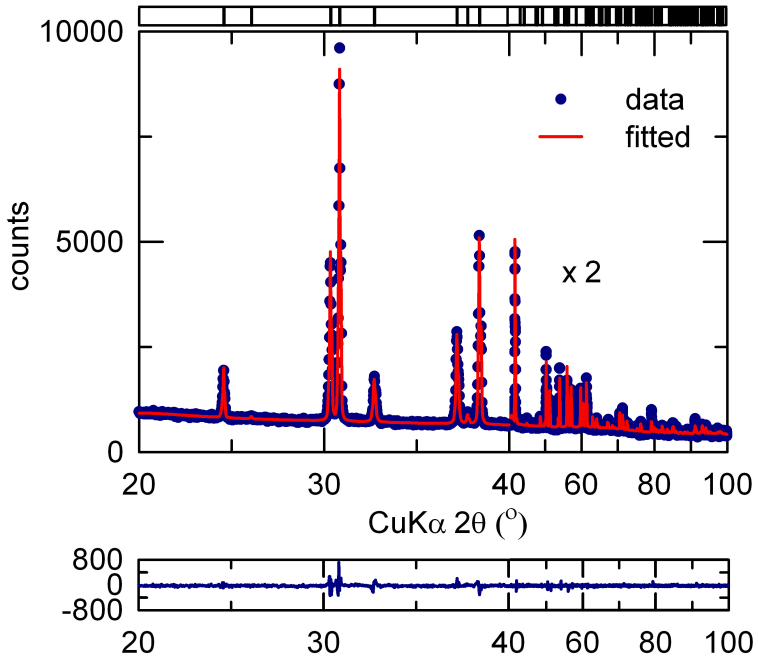

Figure S2: Results of Rietveld refinement of the crystal structure of $Sr_{2.975}Ce_{0.025}Al_{0.5}Si_{0.5}O_{4.5}F_{0.5}$ ($x = 0.5$) using X-ray diffraction data. Vertical lines at the top of the panel indicate expected peak positions for SASF:Ce^{3+} ($x = 0.5$) and difference profiles are displayed.

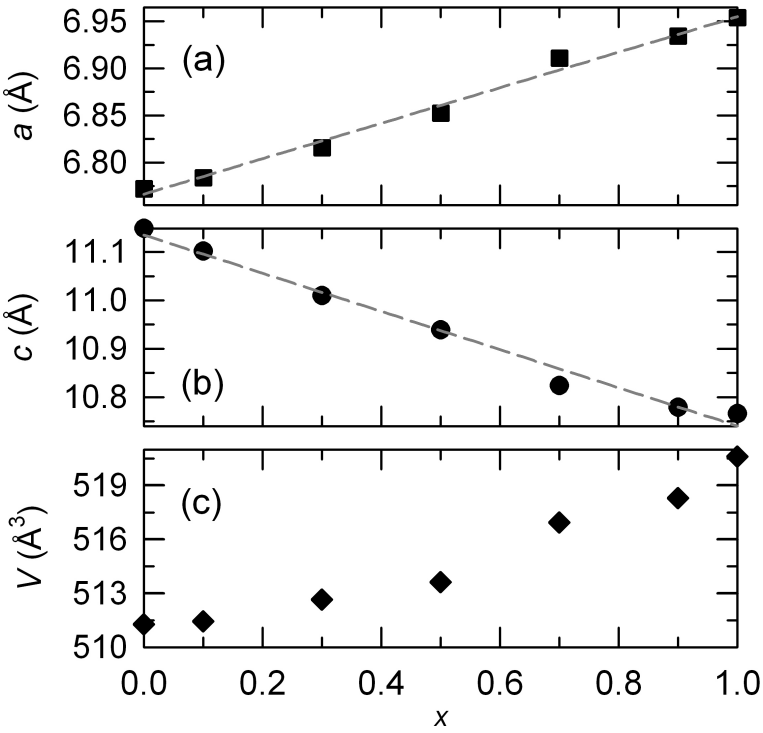

Figure S3: Lattice parameters and cell volume of the $Sr_{2.975}Ce_{0.025}Al_{1-x}Si_xO_{4+x}F_{1-x}$ phosphor (x = 0, 0.1, 0.3, 0.5, 0.7, 0.9, and 1.0) as a function of x as obtained from Rietveld refinement of XRD data: (a) a-axis, (b) c-axis, and (c) cell volume for different x values. Gray dashed lines are the best linear fits.

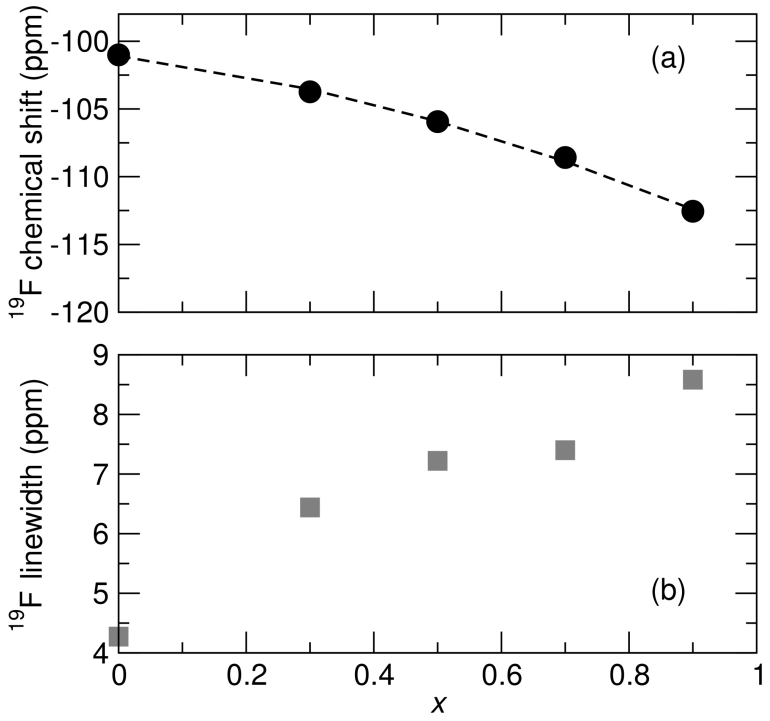

Figure S4: ^{19}F NMR (a) isotropic chemical shifts and (b) linewidths as a function of x for the $Sr_{2.975}Ce_{0.025}Al_{1-x}Si_xO_{4+x}F_{1-x}$ phosphor.

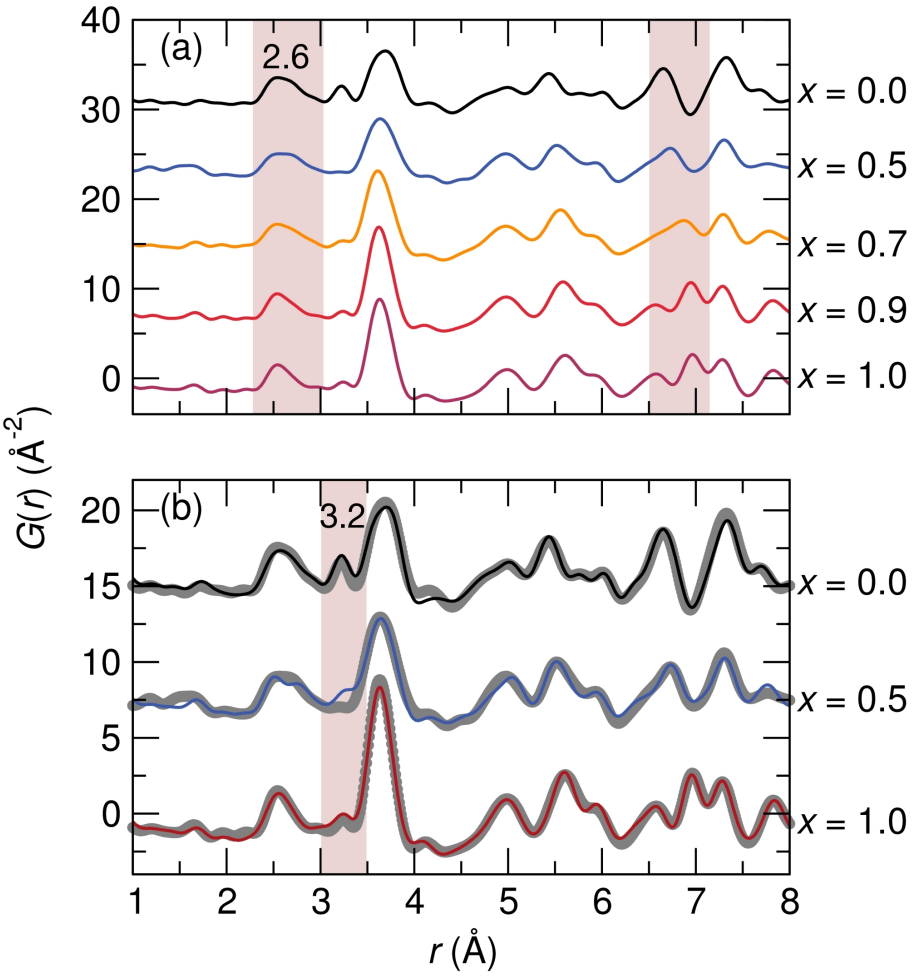

Figure S5: (a) Progression of the experimental pair distribution functions extracted from synchrotron diffraction data. The values of x in $Sr_{2.975}Ce_{0.025}Al_{1-x}Si_xO_{4+x}F_{1-x}$ are indicated. (b) Fits to the PDF using the average crystal structures for materials with $x = 0.0$, 0.5, and 1.0.

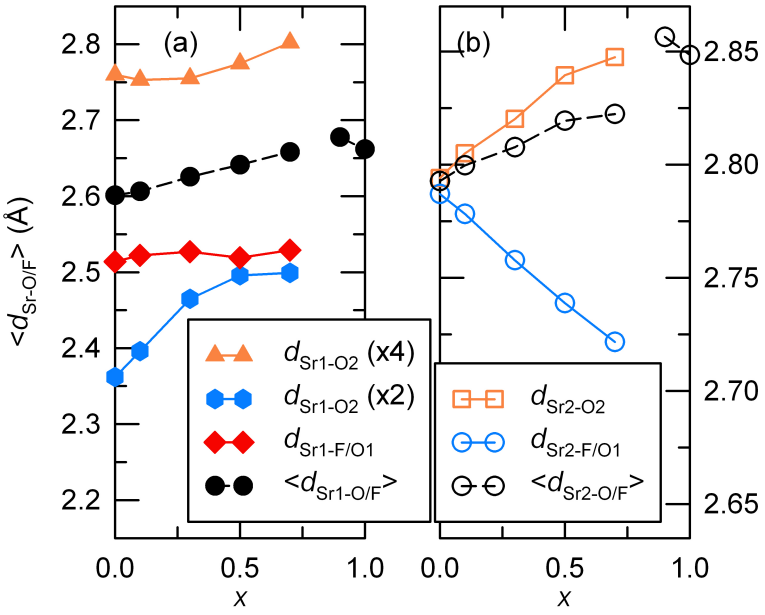

Figure S6: Mean Sr–O/F atomic distances obtained from Rietveld refinements of different $Sr_{2.975}Ce_{0.025}Al_{1-x}Si_xO_{4+x}F_{1-x}$ materials (x = 0, 0.1, 0.3, 0.5, 0.7, 0.9, and 1.0) for each Sr1 and Sr2 polyhedron: (a) Sr1–O/F and (b) Sr2–O/F. Number of bonds are given in parentheses.

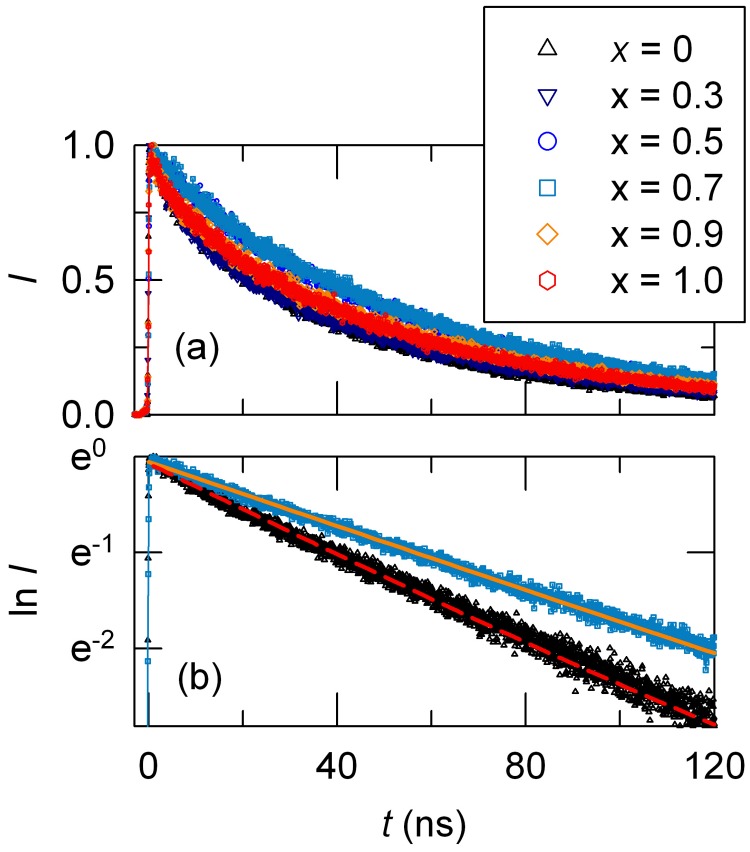

Figure S7: (a) Luminescence decay profiles of $Sr_{2.975}Ce_{0.025}Al_{1-x}Si_xO_{4+x}F_{1-x}$ for x = 0, 0.3, 0.5, 0.7, 0.9, and 1.0 after excitation at 405 nm at room temperature: (b) Fits to a single exponential function for materials with the shortest (x = 0.0) and the longest (x = 0.7) lifetimes.

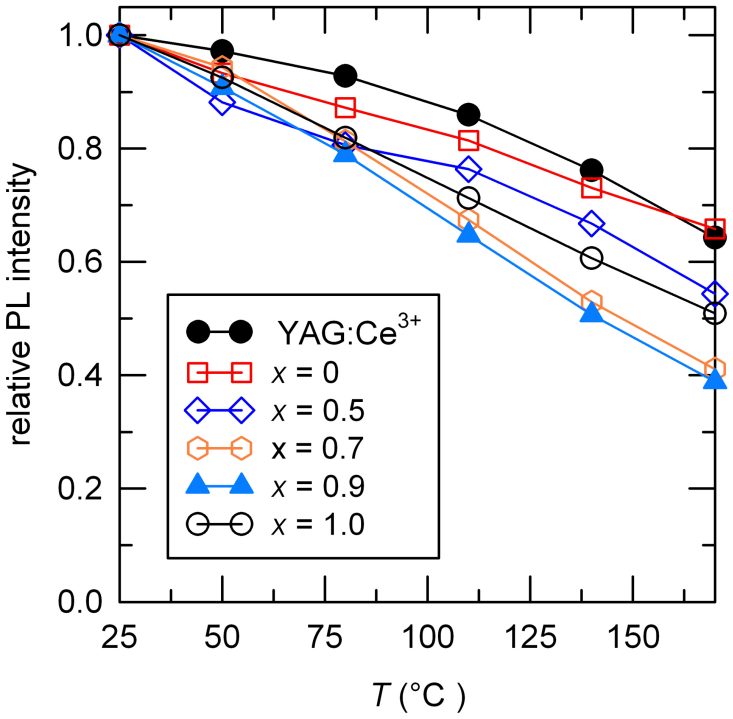

Figure S8: PL intensities for thermal quenching of commercial YAG:Ce^{3+}, $Sr_{2.975}Ce_{0.025}Al_{1-x}Si_xO_{4+x}F_{1-x}$ (x = 0, 0.5, 0.7, 0.9, and 1.0) in the temperature range from 25 to 170 °C.